frontiers | Frontiers in Energy Research

ORIGINAL RESEARCH
published: 06 July 2022
doi: 10.3389/fenrg.2022.964011

Insights Into the Template Effect on Nanostructured CuO Catalysts for Electrochemical CO_2 Reduction to CO

Xiaodong Ye[1], Yangyang Jiang[1], Xi Chen[1,2], Benshuai Guo[1,2], Songbai Mao[1,2], Yafei Guo[3] and Chuanwen Zhao[3]*

[1]Sinopec Nanjing Chemical Industries Co., Ltd., Nanjing, China, [2]Sinopec Nanjing Research Institute of Chemical Industry Co., Ltd., Nanjing, China, [3]School of Energy and Mechanical Engineering, Nanjing Normal University, Nanjing, China

Electrochemical CO_2 reduction to CO using copper-based catalysts has been recognized a promising approach to realizing anthropologic carbon cycle. However, copper-based catalysts face the challenges of low reduction activity and poor selectivity in CO_2 reduction reaction. Tuning particle size and oxygen vacancy represents an efficient strategy for boosting their activity and selectivity. Herein, we reported the preparation of nanostructured CuO catalysts for selective electrochemical CO_2 reduction to CO. Several templates were employed in the template-assisted hydrothermal process to regulate the particle size and oxygen vacancy. Structure-property-activity relationships of the CuO nanostructures depend on the template effect. CuO-PVP and CuO-SDS synthesized using polyvinylpyrrolidone (PVP) and sodium dodecyl sulfate (SDS) as templates exhibited smaller particles sizes and higher concentrations of oxygen vacancy defects. Under the applied potential of −0.93 V vs. RHE, the desired CuO-PVP and CuO-SDS catalysts exhibited good CO_2 reduction activity with high electrochemical surface area normalized partial current density of 2.21 and 1.37 mA/cm^2 for CO production and outstanding CO selectivity with high faradaic efficiencies of 48.2 and 50.5%. Density functional theory (DFT) calculations indicated that oxygen vacancies in the CuO nanostructures not only promoted CO_2 adsorption and activation but facilitated CO desorption from the catalyst surface, and therefore boosted the activity and CO selectivity in CO_2 reduction. The results have deepened the understanding of the structure-property-activity relationships of CuO catalysts, and these will provide guidance for designing highly efficient and robust catalysts for electrochemical CO_2 reduction to CO.

Keywords: template-assisted hydrothermal synthesis, CuO nanostructures, electrochemical CO_2 reduction, particle size effect, oxygen vacancy

OPEN ACCESS

Edited by:
Tao Wang,
Zhejiang University, China

Reviewed by:
Changlei Qin,
Chongqing University, China
Yingjie Li,
Shandong University, China

****Correspondence:***
Yafei Guo
yfguo@njnu.edu.cn

Specialty section:
This article was submitted to Carbon Capture, Utilization and Storage, a section of the journal Frontiers in Energy Research

Received: *08 June 2022*
Accepted: *16 June 2022*
Published: *06 July 2022*

Citation:
Ye X, Jiang Y, Chen X, Guo B, Mao S, Guo Y and Zhao C (2022) Insights Into the Template Effect on Nanostructured CuO Catalysts for Electrochemical CO_2 Reduction to CO. Front. Energy Res. 10:964011. doi: 10.3389/fenrg.2022.964011

INTRODUCTION

The increasing energy crisis and environmental issues caused by the greenhouse gas emissions are the great challenges ahead for human beings. CO_2 capture and utilization (CCU) is expected to alleviate the energy and environmental crisis to achieve a carbon-neutral society (Mac Dowell et al., 2017; Guo et al., 2020a; Guo et al., 2020b). Developing renewable energy can also be an effective approach, whereas wind and solar power can hardly overcome their volatility and intermittency (Xu et al.,

2019). In this framework, electrochemical reduction of CO_2 into value-added products using the off-grid power could be an effective strategy toward carbon cycle and clean energy storage (Gattrell et al., 2007; Jhong et al., 2013; Yang et al., 2018).

The electrochemical CO_2 reduction (ECR) is a complex process that involves multi-electron transfer reaction pathways, and the products would include CO, formic acid, methanol, formaldehyde, methane, ethylene, ethanol and acetate (Sun et al., 2017; Dai et al., 2019; Wang et al., 2021a; Wang et al., 2021b; Liu et al., 2021). ECR into CO through a two-electron reduction process has attracted broad attention, since CO is an important feedstock for synthesizing valuable commodity chemicals and carbon-based alternative fuels (Zhang et al., 2020a; Lu et al., 2020; Chen et al., 2021). Designing highly efficient catalysts is essential for ECR process (Dongare et al., 2020; Kou et al., 2020).

Cu-based catalysts have been highlighted as promising candidates for ECR into chemicals and fuels (Gu et al., 2018). However, low reduction activity and poor product selectivity in ECR remain as challenges. So far, it requires a high potential (−1.0 V vs. RHE) for ECR over Cu-based catalysts, and the CO selectivity is far from expectation. For example, the monocrystal and polycrystal Cu electrodes exhibited high reduction potentials of −1.55~-1.05 V vs. RHE and low CO faradaic efficiencies of 0.9–2.0% in 0.1 M saturated $KHCO_3$ electrolyte (Hori et al., 1989; Hori et al., 2003; Kuhl et al., 2012). Cu nanoparticles (NPs), Cu nanowires (NWs) and Cu foam also showed low CO faradaic efficiencies under the applied potentials of −0.6~−1.10 V vs. RHE (Tang et al., 2012; Ma et al., 2015; Dutta et al., 2017). There is still much room for improving their catalytic performance in ECR. Hence, it is critically necessary to design efficient Cu-based catalysts with higher CO selectivity for ECR application.

Previous contributions have highlighted that the atomic structure and electron configuration of Cu-based catalysts would affect their ECR performance. Cu atoms located at the corner, edge and plane of the crystal own different coordination numbers and energy barriers, and the nanostructured Cu-based electrodes exhibit tunable ECR properties (Birhanu et al., 2018; Xie et al., 2018; Nitopi et al., 2019). Iyengar et al. prepared octahedral-structure Cu crystals with varied grain sizes, and the Cu atoms located at the corner and edge positions determined the ratios of (100)/(111) and (110)/(111) defects, and CH_4 selectivity would thus be affected (Iyengar et al., 2019). ECR performance of Cu nanostructures has also been reported to be associated with particle size effect. Cu nanostructures with smaller grain sizes are preferential for the formation of CO. In contrast, the increase in particle size favors the formation of CH_4 and C_{2+} products (Reske et al., 2014). Thus, it is desirable to tailor the particle size of Cu-based electrode for enhanced CO selectivity.

Efforts have been made to prepare Cu-based catalysts with varied particle sizes by using the template-assisted electro deposition, pulse, thermal annealing, inverse micelle encapsulation, and hydrothermal synthesis methods (Li and Kanan, 2012; Reske et al., 2014; Dutta et al., 2016; Huang et al., 2017; Larrazábal et al., 2017). Amongst, hydrothermal synthesis method is facile and effective for tailoring the morphology and particle size of nanostructured catalysts. Nanostructured CuO catalysts with different morphologies have been synthesized using water-bath process in published documents (Huang et al., 2017). The morphology and electrochemical activity of the CuO nanostructures are closely associated with the configuration of the raw materials and water-bath conditions (Huang et al., 2017). Templates as structure-directing agents, play important roles in tuning the particle size of CuO nanostructures in hydrothermal synthesis. So far, the template effect on the particle size and ECR performance of CuO nanostructures has been rarely reported.

Herein, we prepared CuO nanostructures via hydrothermal synthesis using different templates. The objective of the work is to illustrate the effect of template on the structure-property relationships of the CuO nanostructures in electrochemical CO_2 reduction. CuO-PVP (polyvinylpyrrolidone) and CuO-SDS (sodium dodecyl sulfate) show good CO selectivity with high faradaic efficiencies of 48.2 and 50.5% at −0.93 V vs. RHE. Characterization results and density functional theory (DFT) calculations evidence that the enhanced catalytic activity for CO is associated with the minimized particle sizes and abundant oxygen-vacancy defects.

EXPERIMENTAL SECTION

Raw Materials

Copper chloride dihydrate ($CuCl_2{\cdot}2H_2O$, 99.99%) was employed as copper precursor. Polyvinyl pyrrolidone (PVP, M_w = 10,000)), sodium dodecyl sulfate (SDS, 99.0%), PEO-PPO-PEO triblock copolymer Pluronic F127 (M_w = 12,600, PEO = 70 wt%) and PEG-PPG-PEG triblock copolymer Pluronic P123 (M_w = 5,800, PEG = 30 wt%) were employed as templates. $NH_3{\cdot}H_2O$ solution (≥25% in H_2O) and sodium hydroxide (NaOH, 99.9%) were selected as precipitant and pH modifier, respectively. Nafion 117 solution (5 wt% in a mixture of lower aliphatic alcohols and water) was employed as glue for catalyst coating. All the reagents were purchased from Aladdin Industrial Corporation, and they were used as received.

Preparation of CuO Nanostructures and Electrodes

CuO nanostructures were prepared by template-assisted hydrothermal synthesis method (Huang et al., 2017). First, 0.9 g of $CuCl_2{\cdot}2H_2O$ and 0.3 g of template were added to 100 ml of deionized water, and they were stirred to form uniform solution. 2 ml of $NH_3{\cdot}H_2O$ solution was added to the solution followed by ultrasonic treatment for 15 min. Next, 1.0 M NaOH solution was added dropwise to the mixture under stirring to form light blue precipitate. The mixture was then aged at room temperature overnight and the resulting precipitate was separated by filtration and dried at 60°C for 5 h, followed by calcination at 400°C for 2 h. The CuO nanostructures prepared by using different templates were labelled as CuO-PVP, CuO-SDS, CuO-F127 and CuO-P123, respectively. 0.02 g of the prepared CuO nanoparticles (NPs) were mixed with 80 μl of deionized

water and 40 μl of Nafion 117 solution, and the mixture was subjected to ultrasonic treatment for 10 min. The obtained slurry was uniformly coated on 1 cm × 1 cm carbon paper and dried by cold air to prepare CuO electrodes.

Characterization

Nitrogen adsorption-desorption measurements at 77 K were performed using a Micromeritics ASAP 2460 instrument, and physical parameters of specific surface area and porosity were obtained. Powder X-ray diffraction (XRD) was conducted with a Bruker D8 ADVANCE instrument operated at 40 kV and 40 mA with nickel filtered Cu Kα radiation (wave length of 0.15406 nm). Field emission scanning electron microscopy (FESEM) measurements were performed using a JSM7800F microscope operated at 10.0 kV. High resolution transmission electron microscopy (HRTEM) measurements were carried out using a FEI TECNAI G2 F20 microscope. X-ray photoelectron spectroscopy (XPS) was conducted with an ESCALAB 250Xi spectrometer using Al Kα radiation.

Electrochemical Measurements

The electrochemical reduction of CO_2 was carried out using a three-electrode electrochemical cell configuration coupled with a CHI660E workstation and a gas chromatograph (GC). The three-electrode system was composed of Ag/AgCl as reference electrode, platinum filament as counter electrode and glassy carbon as working electrode. The cathode and anode chambers of the H-type cell were separated by a Nafion117 proton exchange membrane.

Pure CO_2 was purged into the 0.1 M $KHCO_3$ electrolyte at a flow rate of 40 ml/min for 30 min to remove residual air before electrolysis. Linear sweep voltammetry (LSV) tests were conducted under the potential of −1.6–0 V vs. Ag/AgCl with a scan rate of 50 mV/s. The applied potentials were recorded relative to the Ag/AgCl reference electrode, and they were converted to the RHE scale accroding to **Eq. 1** (Abdi and van de Krol, 2012):

$$V_{RHE} = V_{Ag/AgCl} + V^0_{Ag/AgCl\ vs\ NHE} + 0.059pH \quad (1)$$

where $V^0_{Ag/AgCl\ vs\ NHE}$ is 0.199 V at 25°C, V_{RHE} is the potential vs. reversible hydrogen electrode (RHE).

Electrochemical impedance spectroscopy (EIS) tests were carried out at the frequency of 0.01~10^6 Hz with an amplitude of 5 mV. Potentiostatic electrolysis tests were conducted at the desired potential by delivering CO_2 continuously to the cathode compartment for 75 min, and the gaseous products were detected by online GC. The faradaic efficiency (FE) of gaseous products were calculated using **Eq. 2** (Han et al., 2017):

$$FE = \frac{N \times F \times C_i \times v \times P}{j \times R \times T} \quad (2)$$

where j is current density (A), FE is Faradic efficiency, F is the Faraday constant (96,500 C/mol), N is the number of electron transferred, C_i is the concentration of product i (mol/L), v is the gas flow rate (m^3/s), P is pressure (Pa), R is the ideal gas constant (8.314 J/(molK)) and T is temperature (K).

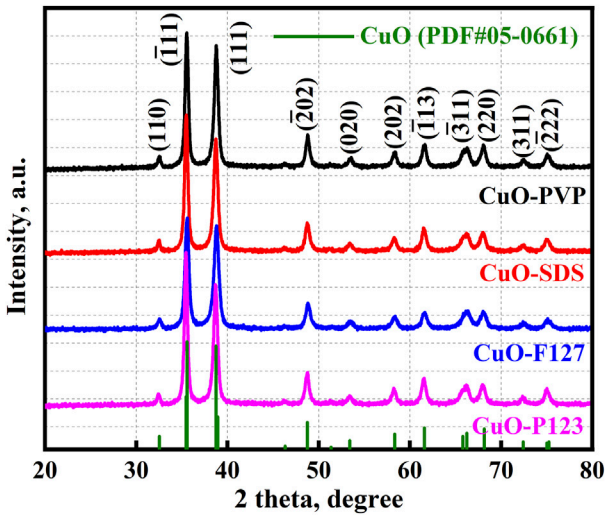

FIGURE 1 | XRD patterns of the CuO catalysts synthesized with different templates.

Determination of Electrochemical Active Surface Area

The surface roughness factor and electrochemically active surface areas (ECSA) of the catalysts were evaluated by measuring the double-layer capacitance (C_{dl}). Cyclic voltammetry (CV) tests were carried out in 0.1 M $KHCO_3$ electrolyte at various scan rates of 5–50 mV/s. The capacitive currents (ΔJ) against the scan rate were plotted and the C_{dl} was calculated as the slope of the fitting line. ECSA was then calculated by dividing the C_{dl} by the capacitance of ideal CuO with smooth surface (usually taken as 40 μF/cm^2), as shown in **Eq. 3** (Zhao et al., 2020):

$$ECSA = \frac{C_{dl}}{40\ \mu F/cm^2} \quad (3)$$

DFT Calculations

DFT calculations were performed by using the CASTEP program in Materials Studio. Generalized gradient approximation (GGA) of the Perdew–Burke–Ernzerhof (PBE) exchange-correlation functional method was employed for calculation, and the cutoff energy was set to 500 eV. The monoclinic-CuO (111) facet was modeled by (3 × 3) supercell with one Cu-O layer. A customized (3 × 3 × 1) Monkhorst-Pack grid of k-point was sampled. More details about the calculation of free energy can be found in the Supporting Information.

RESULTS AND DISCUSSION

Structural and Morphological Analysis

Physical properties of the CuO nanostructures prepared with different templates are characterized by N_2 adsorption-desorption technique. **Supplementary Figure S1** depicts the N_2 adsorption-desorption isotherms and pore size

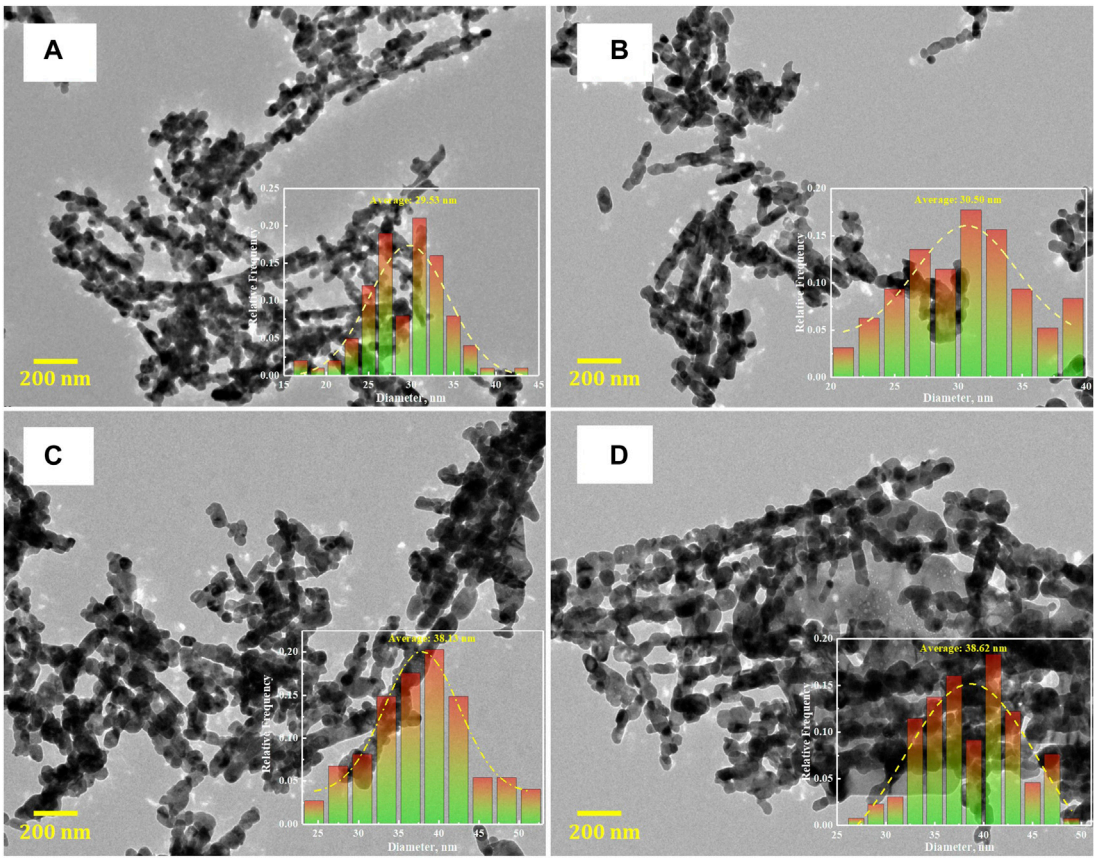

FIGURE 2 | HRTEM images of the CuO catalysts synthesized with different templates. **(A)** CuO-PVP; **(B)** CuO-SDS; **(C)** CuO-F127; **(D)** CuO-P123.

distributions, and their textural parameters are summarized in **Supplementary Table S1**. All the catalysts present Type IV isotherms with Type H3 hysteresis loops located in the P/P_0 = 0.8–1.0, which implies that they are mesoporous materials containing slit pores due to particle packing (Sing, 1985). The catalysts show bimodal pore size distribution, with majority of the pores centering at 3 and 55 nm. Besides, the catalysts show no much difference in their specific surface areas and total pore volumes, indicating that template exerts no significant effect on their textural parameters.

Crystalline structures of the different CuO nanostructures are identified by XRD analysis, and the XRD patterns are depicted in **Figure 1**. The catalysts show repeated diffraction peaks at the 2θ positions of 32.5°, 35.5°, 38.8°, 48.8°, 53.5°, 58.3°, 61.6°, 66.2°, 68.0°, 72.5° and 75.1°, which are associated with the (1 1 0), (1 (_) 1 1), (1 1 1), (2 (_) 0 2), (0 2 0), (2 0 2), (1 (_) 1 3), (3 (_) 1 1), (2 2 0), (3 1 1), and (2 (_) 2 2) facets of the monoclinic CuO (JCPDS #05–0661) (Jiang et al., 2021). The diffraction peaks of high intensity at the 2θ positions of 35.5° and 38.8° imply good crystallinity for the catalysts. No diffraction peaks of metallic Cu and Cu_2O could be discerned, indicating that the catalysts retain stable CuO phase. To provide more quantitative analysis, unit cell refinement was performed using all reflections, the average crystalline sizes were calculated using the Scherrer equation, and the crystallinity was calculated from peak integration. As indicated in **Supplementary Table S1**, all the CuO catalysts exhibit high degree of crystallinity (0.90–0.92), and the crystallinity shows no much difference amongst the different catalysts. This indicates that template exert no significant effect on their crystallinity. The standard cell parameters for the pure monoclinic CuO (PDF#05-0661) are a = 4.684 Å, b = 3.425 Å, and c = 5.129 Å. In contrast, cell parameters of the different CuO catalysts are slightly higher than those of the pure monoclinic CuO, indicating that the presence of template in hydrothermal synthesis has resulted in crystal distortion. The XRD profiles with local zoom inset in **Figure 1** indicate that the diffraction peaks of CuO-PVP, CuO-SDS and CuO-F127 at 35.5° and 38.8° slightly shift toward higher 2θ positions, which provides evidence for crystal distortion of the CuO catalysts. Moreover, the average crystalline sizes of the different CuO catalysts are calculated to be 15.68, 18.91, 19.32, and 19.87 nm, respectively. The difference in their crystalline size might be associated with the fact that the templates will influence in varying degrees on nucleation and crystal growth of CuO in hydrothermal synthesis. Particularly, the desired CuO-PVP catalyst exhibit minimum crystal size, which would be conducive to promoting

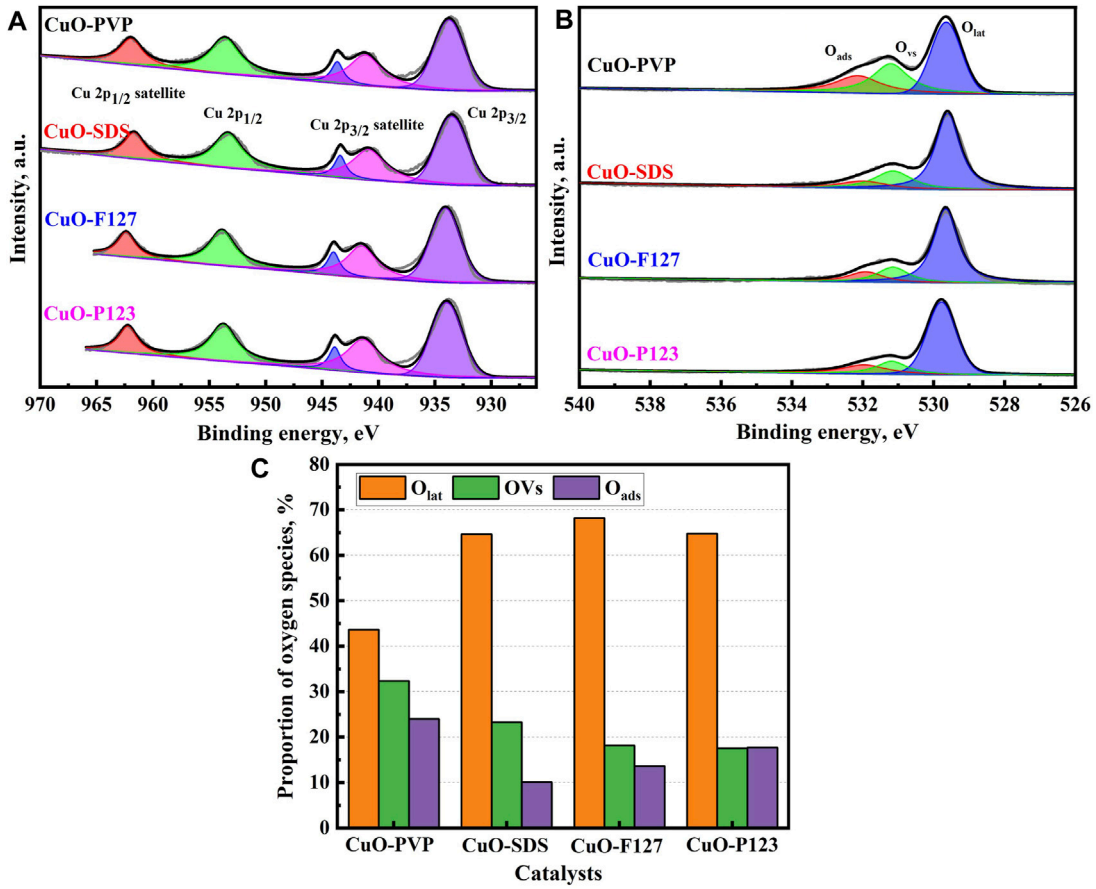

FIGURE 3 | XPS profiles of the CuO catalysts synthesized with different templates. **(A)** Cu 2p; **(B)** O 1s; **(C)** distribution of oxygen species.

electrochemical performance by providing more active surface sites.

Surface morphologies of the different CuO nanostructures are characterized by FESEM and HRTEM. The FESEM images in **Supplementary Figure S2** show that the structures of the CuO-PVP, CuO-F127 and CuO-P123 catalysts are nanorod-like, aggregated by CuO NPs, and a large number of CuO NPs are attached to the surface of the rod-like structures. For the CuO-SDS catalyst, a large number of CuO NPs are evenly distributed on the surface, and only a few rod-like structures could be observed from the FESEM images. The TEM images in **Figure 2** show that the average particle sizes of the CuO nanostructures are 29.53, 30.50, 38.13, and 38.62 nm, respectively. The HRTEM images in **Supplementary Figure S3** show lattice fringes with an inter-planar d-spacing of 0.236 nm, which are assigned to the (1 1 1) plane of CuO (JCPDS #05-0661) (Jiang et al., 2021). In addition, the selected area electron diffraction (SAED) images also evidence the presence of (1 1 1) plane. Overall, the CuO nanostructures show subtle difference in their surface morphologies, while they exhibit obvious variation in average particle size, and this might affect their ECR performance.

The chemical compositions and elemental valence of the CuO nanostructures are determined by XPS analysis. **Figure 3** shows the core-level XPS spectra of Cu 2p and O 1s of the different CuO catalysts. As depicted in **Figure 3A**, characteristic peaks for Cu $2p_{1/2}$ and Cu $2p_{3/2}$ can be observed at the binding energies of 953.8 and 933.8 eV. Besides, characteristic peak for Cu $2p_{1/2}$ satellite can also be found at 962.0 eV. The peaks present at 943.6 and 941.1 eV are assigned to Cu $2p_{3/2}$ satellite. Furthermore, the characteristic peaks for Cu $2p_{1/2}$ and Cu $2p_{3/2}$ show symmetric distribution with a peak separation of around 20.0 eV, and the peak positions and separation match are consistent with those of the standard CuO spectrum. These results indicate that Cu (II) is the major valence state for copper species (Tan et al., 2020). **Figure 3B** shows that the high-resolution O 1s spectra of the CuO catalysts can be deconvoluted into three peaks. The characteristic peaks at the binding energies of 529.7, 531.4 and 532.2 eV are associated with lattice oxygen (O_{lat}), O atoms adjacent to oxygen vacancies (OVs) and surface adsorbed oxygen (O_{ads}), respectively (Al-Hashem et al., 2019; Tan et al., 2020; Zhuang et al., 2020). The present peak at the binding energy of 531.4 eV should signify the presence of oxygen vacancy defects in the CuO catalysts and the oxygen vacancies concentration can be estimated from the

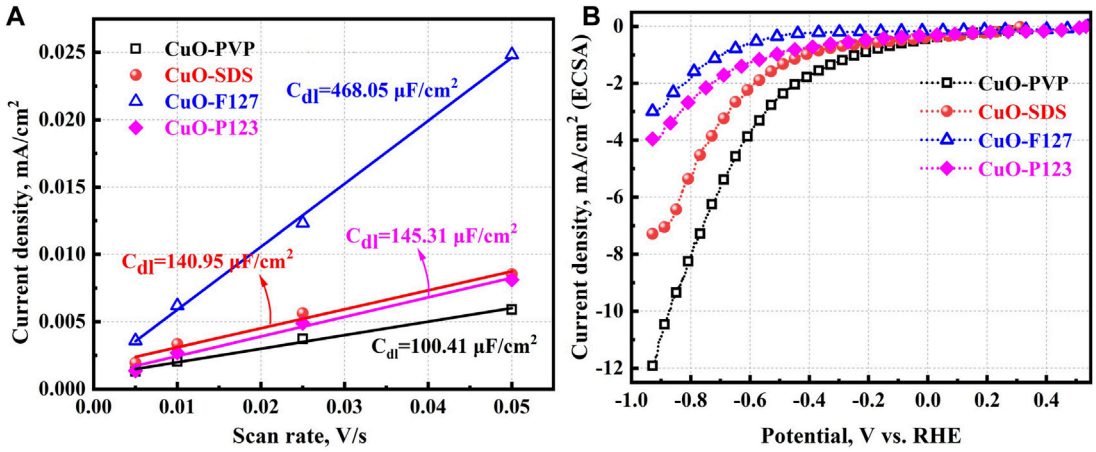

FIGURE 4 | (A) Determination of double layer capacitance. **(B)** LSV curves of the CuO nanostructures in 0.1 M $KHCO_3$ saturated with CO_2.

corresponding OVs peak area ratio (OVs% = OVs/(O_{lat} + OVs + O_{ads})).

Chemical compositions of the CuO nanostructures are summarized in **Supplementary Table S2**. As indicated, CuO-PVP shows a lower surface atomic concentration for Cu 2p, while its surface atomic concentration for O 1s is relatively higher. The distribution of oxygen species in the different CuO nanostructures is further depicted in **Figure 3C**. The O_{lat}, OVs and O_{ads} in CuO-PVP account for 43.64, 32.35 and 24.01%, indicating that the oxygen species are uniformly distributed. Nevertheless, lattice oxygen is the major oxygen species for CuO-SDS, CuO-F127 and CuO-P123, since O_{lat} accounts for more than two-thirds in the total oxygen species. The concentrations of oxygen vacancies for the different CuO catalysts are calculated as 32.35, 23.26, 18.17 and 17.55%, respectively. Notably, the oxygen vacancies concentration shows obvious difference among the various CuO catalysts. It should be noted that oxygen vacancy defects play important roles in promoting CO_2 adsorption and activation, and it would be rather difficult to boost oxygen vacancies concentration drastically. Jiang et al. employed the metal oxide doping strategy to increase oxygen vacancies concentration of CuO for enhanced C_2H_4 production in CO_2RR. Upon SnO_2 doping, oxygen vacancies concentration (the ratio of vacancy oxygen and lattice oxygen) can be increased from 34 to 45% (Jiang et al., 2021). Jiang et al. prepared Pt/CeO_2 catalysts with tunable oxygen vacancies density and morphologies, and the density of Ov ranks in the following order: 2Pd/CeO_2-R (0.48) > 2Pd/CeO_2-P (0.31) > 2Pd/CeO_2-C (0.28) > 2Pd/CeO_2-O (0.24) (Jiang et al., 2020). The desired CuO-PVP catalyst shows the highest oxygen vacancies concentration of 32.35%, which is comparable to or higher than those of the similar catalysts reported in literatures. These observations imply that the varied oxygen vacancy concentrations amongst the CuO catalysts might be associated with their ECR performance.

Investigation of Electrochemical CO_2 Reduction

To study the intrinsic activity of the different CuO nanostructures, their current densities should be normalized by ECSA. Therefore, the catalysts are tested in N_2-saturated 0.1 M $KHCO_3$ electrolyte at the scan rate of 5–50 mV/s, and the CV curves are presented in **Supplementary Figure S4**. The slope of the fitting lines in **Figure 4A** further provides the double layer capacitances (C_{dl}), and the capacitances are 100.41, 140.95, 468.05, and 145.31 μF/cm^2 for the CuO-PVP, CuO-SDS, CuO-F127, and CuO-P123, respectively. The ECSA values of the different CuO nanostructures are thus determined as 2.51, 3.52, 11.70, and 3.63. The different capacitances and ECSA values should indicate that the varied templates will affect the surface roughness of the catalysts. Electrochemical performance of the CuO nanostructures is further evaluated by testing the catalysts in CO_2-saturated 0.1 M $KHCO_3$ electrolyte at the potentials of −0.93–0.67 V vs. RHE. The ECSA normalized current densities of the catalysts are displayed in **Figure 4B**. CuO-PVP and CuO-SDS also show higher ECSA normalized current densities than CuO-F127 and CuO-P123. For instance,

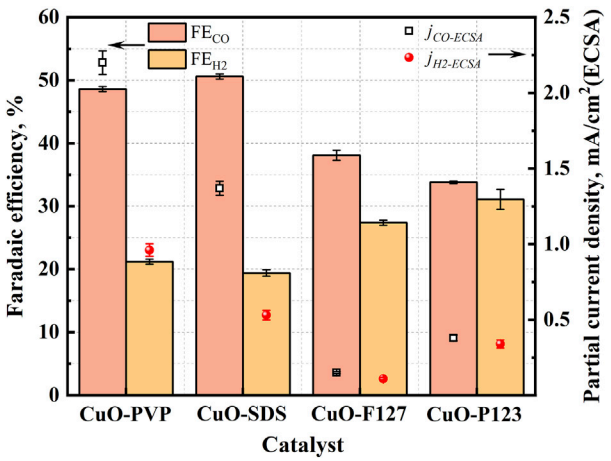

FIGURE 5 | Faradaic efficiencies of CO and H_2 and partial current densities normalized to ECSA for the CuO nanostructures tested at −0.93 V vs. RHE.

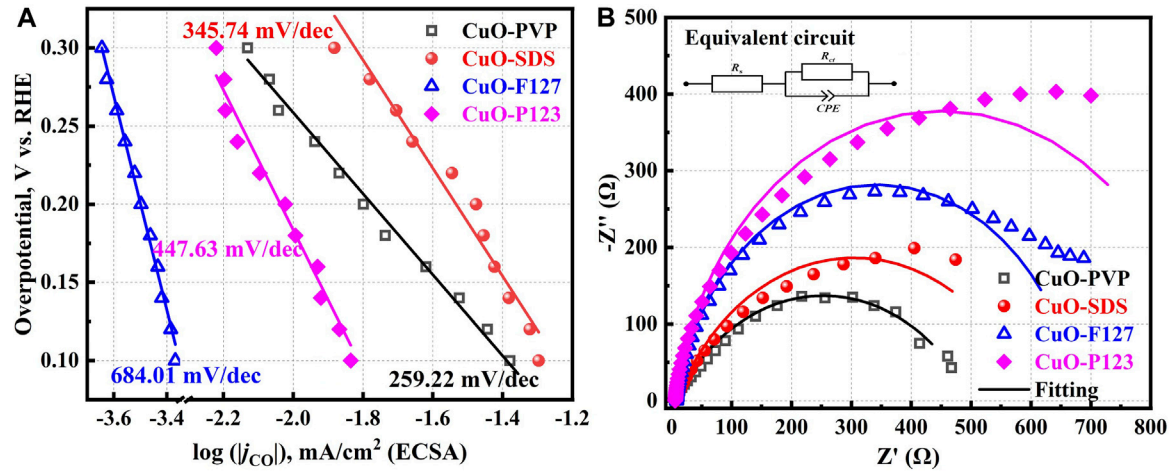

FIGURE 6 | (A) CO partial current density Tafel plots. **(B)** Nyquist plots.

the ECSA normalized current densities of CuO-PVP and CuO-SDS at the applied potential of −0.93 V vs. RHE are as high as −11.92 and −7.28 mA/cm^2, which indicates that they show higher specific reduction activity. The catalysts have also been tested in N_2-saturated 0.1 M $KHCO_3$ electrolyte to study the hydrogen evolution reaction (HER) performance. As depicted in **Supplementary Figure S5**, the CuO nanostructures exhibit lower ECSA normalized current densities in N_2-saturated electrolyte than in the CO_2-saturated environment. This indicates that the CO_2 reduction reaction (CO_2RR) prevails over HER in the ECR process.

Faradic efficiencies and ECSA normalized partial current densities of the gaseous products are shown in **Figure 5**. Under the applied potential of −0.93 V vs. RHE, CuO-PVP and CuO-SDS show much higher FEs for CO (48.2 and 50.5%), and their FEs for H_2 are relatively lower (21.1 and 19.4%). The CO/H_2 ratios for CuO-PVP and CuO-SDS are close to 2.0, while those for CuO-P127 and CuO-P123 approximate 1.0, indicating that the CuO nanostructures prepared with different templates yield syngas with tunable CO/H_2 ratios. Besides, compared to CuO-F127 and CuO-P123, the ECSA normalized partial current densities of CO ($j_{CO\text{-}ECSA}$) for CuO-PVP and CuO-SDS are greater (2.21 and 1.37 mA/cm^2). To better clarify the precision of the experimental data, each test has been repeated for three times, and the relative error retains within 5%. The experimental data have been analyzed by analysis of variance (ANOVA), and the results of one-way ANOVA for CO and H_2 FEs are summarized in **Supplementary Tables S3, S4**. Results indicated that the inter-block variation is more significant than the inter-class variation for CO and H_2 selectivity, implying that the different templates exert obvious effect on the products selectivity, while the repeating tests show low error.

Tafel analysis is performed to investigate the interfacial reaction kinetics. The applied potentials are prudently selected in the Tafel regime to avoid the mass transport limitations. The Tafel plots for CO formation in **Figure 6A** show that the Tafel slopes of the CuO nanostructures are 259.22, 345.74, 684.01, and 447.63 mV/dec. The CuO-PVP and CuO-SDS catalysts exhibit much lower Tafel slopes than CuO-F127 and CuO-P123, as an indicative of relatively faster kinetics for CO_2 reduction. EIS tests have also been conducted to analyze the charge-transfer resistances of the different CuO catalysts. The typical EIS diagram in **Supplementary Figure S6** indicates that the ECR over CuO is jointly controlled by charge transfer process (kinetic control) and diffusion process (mass transfer control). Particularly, the diffusion impedance can be neglected since charge transfer resistance is the major barrier that needs to be overcome. The EIS data are fitted with the equivalent circuit model, and the fitted Nyquist plots are depicted in **Figure 6B**. The internal resistance (R_S) and charge-transfer resistance (R_{CT}) of the CuO catalysts determined from the impedance spectroscopy are

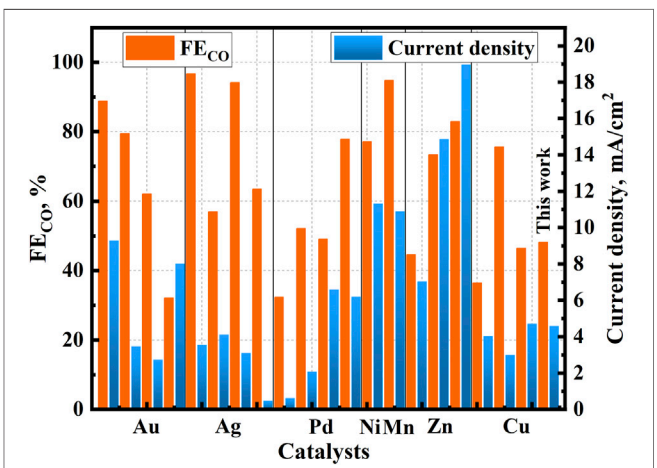

FIGURE 7 | FE_{CO} and total current densities of the different catalysts reported in literatures for ECR to CO.

summarized in **Supplementary Table S5**. Notably, CuO-PVP and CuO-SDS bore much smaller charge transfer resistance, implying that they own low polarization resistance and fast reaction kinetics for ECR. Overall, the desired CuO-PVP and CuO-SDS nanostructures exhibit higher specific activity, greater CO selectivity and faster reaction kinetics in ECR process.

The ECR performance of the desired CuO-PVP and CuO-SDS nanostructures is compared to those of the similar catalysts in some open documents, and the results are summarized in **Figure 7** and **Supplementary Table S6**. Noble metal catalysts generally show high CO selectivity in ECR due to the low binding energy of CO* on the surface. Besides, the abundant low-coordination edge sites will also endow the catalysts with enhanced reduction activity. Au-TOH-50, PON-Ag and Porous Ag showed good ECR performance with high total current densities of −3.10–−9.28 mA/cm^2 and great FE_{CO} of 88.80–96.69% (Peng et al., 2018; Liu et al., 2019; Yang et al., 2020). Yang et al. reported the particle-size effect on Au nanostructures in ECR, and they found that Au trisoctahedron with smaller particle size of 50 nm (Au-TOH-50) exposed more (2 1 1) facets, which played important roles in stablizing the critical intermediate COOH* for enhanced CO selectivity (Yang et al., 2020). Peng et al. attributed the high activity and CO selectivity of the preferentially oriented nanoparticles (PONs) of metallic Ag (PON-Ag) to the preferential exposure of (1 0 0) and (1 1 0) facets (Peng et al., 2018). The good ECR performance of porous Ag was associated with the fact that the unique hollow porous structure provided high electrochemical surface area and intrinsically higher activity (Liu et al., 2019). Commericial Pd catalysts exhibited moderate activities in ECR, while their CO_2RR activities could be improved by tuning the active sites and compositional design (Zhu et al., 2018; He et al., 2020). These had been evidenced by the improved FE_{CO} of 52.14 and 77.84% for the nitrogen-doped carbon-supported Pd single-atom catalyst (Pd/NC) and flower-like Pd_3Cu alloy (FL-Pd_3Cu) (Zhu et al., 2018; He et al., 2020). The promoted ECR performance of Pd/NC benefited from the stabilization of the adsorbed CO_2 intermediate by the well-dispersed Pd-N_4 single-atom sites (He et al., 2020). The high current density and FE_{CO} of the FL-Pd_3Cu catalyst was associated with the alloy effect (Zhu et al., 2018). Transition metals and their oxides also show promise for ECR applications, while their ECR performance should be further improved. Effective strategies of elemental doping to regulate active sites, surface treatment to create more oxygen vacancies, activation and thermal reduction to control valence state have been employed. Ar and H_2 plasma treatments could afford the a-MnOx-H and V_o-rich ZnO catalysts enriched oxygen vacancies for CO_2 adsorption/activation and promoted charge transfer. The a-MnOx-H and V_o-rich ZnO catalysts thus exhibited excellent CO_2RR activity with high FE_{CO} of 94.80 and 82.97% (Geng et al., 2018; Han et al., 2021). The presented surface oxygen vacancies in Cu_2O-FeO had also been correlated to its enhanced overall catalytic efficiencies in ECR (Woyessa et al., 2021). The Ni- and Fe-loaded nitrogen doped carbon dubbed Ni_xFe_{1-x}-NC catalyst and oxide-derived copper nanowire arrays (OD-Cu NAs) enabled tunable syngas formation in ECR process (Geng et al., 2018; Woyessa et al., 2021). The N-coordinated Fe and Ni sites were identified as the major active sites in Ni_xFe_{1-x}-NC for HER and CO_2RR to CO, and the CO/H_2 ratio could be tuned by adjusting the Ni/Fe ratio in the catalyst (Zhang et al., 2020b). The tunable syngas production over OD-Cu NAs was associated with the formed grain boundaries (GBs) for promoted Cu re-oxidation, and the reaction rates of CO_2RR and HER could be fine-tuned by optimizing the GB density (Wang et al., 2020). The copper nanoparticles-dispersed carbon aerogels (Cu/CA) showed a remarkable FE_{CO} of 75.6%, and this was ascribed to the highly dispersed metallic Cu on the carbon aerogels (Xiao et al., 2019). The desired CuO-PVP catalyst in this work possesses a moderate total current density of −4.59 mA/cm^2 and FE_{CO} of 48.20% at −0.93 V vs. RHE. Compared to the Cu/Au, Pd/C, pristine ZnO, OD-Cu NAs and Cu_2O-FeO catalyst, the desired CuO-PVP catalyst prepared in this work shows a higher CO selectivity. Besides, the desired CuO-PVP catalyst also exhibits higher catalytic activity towards CO_2 reduction than those of the Ag foil, Pd/NC, and OD-Cu catalysts. It is noteworthy that CO selectivity and catalytic activity of the CuO-PVP sample is lower than those of the Au-TOH catalysts (Chen et al., 2017; Geng et al., 2018; Peng et al., 2018; Liu et al., 2019; He et al., 2020; Wang et al., 2020; Yang et al., 2020; Woyessa et al., 2021). However, there is still much room for improving its electrochemical performance by varying the synthetic parameters and the concentration of PVP template in hydrothermal synthesis, and this deserves more efforts in the future work.

Theoretical Analysis

The above results indicate that the structural and morphological properties and ECR performance of the CuO nanostructures depend on the different templates employed. Herein, we have provided a brief illustration and discussion about the correlation between the template effect and the structure-property relationships of the CuO nanostructures. Templates as structure-directing agents, play important roles in tuning the particle size of nanostructures in hydrothermal synthesis. **Figure 8** presents a brief illustration of the template-assisted hydrothermal synthesis process. The templates are dissolved in deionized water to form spherical structure with hydrophilic polyethylene oxide (PEO) groups as shell and hydrophobic polypropylene oxide (PPO) groups as core. When the precursor ($CuCl_2{\cdot}2H_2O$), precipitant ($NH_3{\cdot}H_2O$) and pH modifier (NaOH) are added, the precursor is subjected to hydrolysis and the cations will be adsorbed on the alkane chains of the templates, with the aid of hydrogen bond, electrostatic interaction and coordination bond. Then, rapid nucleation occurs and the cations are oriented to present as linear structure. Afterwards, the templates are removed under medium temperature calcination, during which the templates and cations are decomposed to release CO_2, N_2 and H_2O, and the core-shell structure will be subjected to the forces of expansion. Thus, the linear structure will be torn to form smaller NPs (Chen et al., 2013).

As a structure-directing agent, template plays an important role in hydrothermal synthesis process by promoting the

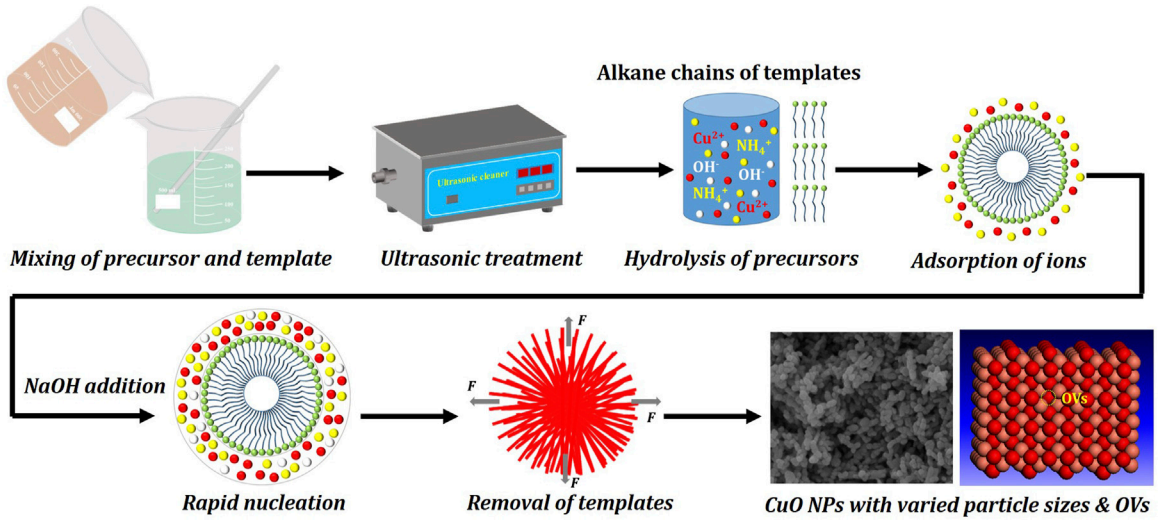

FIGURE 8 | An illustration of the correlation of template effect to particle size and oxygen vacancy defect.

nucleation of nanosized particles (NPs). The template molecules can contact directly with the precursor molecules during the sol-gel procedure, thus preventing the agglomeration of NPs in hydrothermal synthesis (Shu et al., 2014). The template agents used in this paper are PVP, SDS, F127, and P123, respectively. Among them, PVP and SDS are typical polymer surfactant and anionic surfactant, respectively, while F127 and P123 are nonionic surfactants, and the four templates exhibit varied structural properties. PVP represents a typical water-soluble polymer made from the monomer N-vinylpyrrolidone, and the PVP molecule contains pyrrolidone moiety (hydrophilic component) and alkyl group (hydrophobic group). The hydrophobic carbon chains in PVP have benefited the molecules repulsive forces to prevent the aggregation of nanoparticles (NPs). Hence, PVP has been extensively employed as a stabilizing and shape-directing agent in NPs synthesis (Koczkur et al., 2015). SDS is a short-chain anionic surfactant that can easily form reversed micelles in organic solvent. In the reversed micelles, the exterior hydrophobic groups interact with non-polar organic solvent, and the inner hydrophilic groups assemble to form polar core, and the polar core serves as a solubilizer for polar molecules. The restriction of polar core in reversed micelles has restricted the particle size in hydrothermal synthesis. Therefore, SDS has been widely used as the capping agent for synthesizing NPs with controllable sizes (Kuo et al., 2004). The triblock copolymers Pluronic P123 ($EO_{20}PO_{70}EO_{20}$) contains a hydrophilic group of poly (ethylene oxide) (PEO) and a hydrophobic group of poly (propylene oxide) (PPO) (Polak et al., 2021). The triblock copolymers Pluronic F127 ($EO_{106}PO_{70}EO_{106}$) contains a hydrophobic block of polypropylene located between two hydrophilic blocks of polyethylene glycol (Li et al., 2013a). The triblock copolymers in P123 and F127 generally assemble in aqueous solutions to form aggregated micelles. Similar to the reversed micelles formed by SDS, the aggregated micelles feature an inner core containing considerable hydrophobic PPO blocks and several PEO blocks, and an outer shell containing massive PEO blocks. The hydrophobic core of the aggregated micelles has provided a local hydrophobic microenvironment for the directional synthesis of NPs with tunable sizes (Chaibundit et al., 2007). Moreover, all the four templates can be completely removed by calcination at 400°C, implying that no template residues exist in the CuO nanostructures after calcination. Due to the different structural properties and bulk compositions for the templates, their capabilities of forming micelles in solution could be different, and the size of the formed micelles will further affect the average particle size of the CuO nanostructures in the subsequent processes.

However, the CuO-PVP catalyst exhibits good electrocatalytic performance in CO_2RR, which may be related to its grain size, while the abundant –N and C=O functional groups in the PVP template would interact with metal ions via the coordination reaction to form NPs with uniform size. In this process, metal ions are captured by negative charge due to electrostatic attraction, and crystal nucleation and growth occur in the specified direction, and this benefit the formation of catalysts with fixed morphology (Li et al., 2013b). On the other hand, catalysts with minimized particle size and specified morphologies can offer abundant low coordination sites for enhanced catalytic activity in electrochemical CO_2 reduction. Huang et al. fabricated CuO nanostructures by the hydrothermal synthesis method using PVP as template. CuO catalysts with varied morphologies of dumbbell-like nanowires (DBNWs), scattered nanowires (STNWs), microsphere and nanoflake were synthesized by regulating the synthetic parameters. Amongst, the CuO STNWs catalyst exhibited good catalytic performance in electrochemical CO_2 reduction to formate, and the improved catalytic activity was associated with the enriched low coordination sites, one-dimensional structure and great surface area (Huang et al., 2017). Gao et al. prepared Cu_2O catalysts with

varied crystal structures by the template-assisted hydrothermal synthesis. By varying the content of the PVP template, Cu_2O catalysts with different morphologies of cubic (enclosed with 100 facets), octahedral (enclosed with 111 facets) and truncated-octahedral (enclosed with both 111 and 100 facets) structures were fabricated. It was found that the performance of electrochemical CO_2 reduction to ethylene depended on the different crystal facets. The increased PVP content in hydrothermal synthesis favored the formation of truncated-octahedral structured Cu_2O catalyst enclosed with both 111 and 100 facets, and this promoted ethylene production by facilitating C-C coupling and ethylene desorption and enhancing multielectron involved kinetics (Gao et al., 2020). These results indicate that the types of template agents have an influence on the electrocatalytic reduction performance.

Besides, the varied ECR performance amongst the CuO nanostructures have been correlated to the difference in their average particle size and the concentration of oxygen vacancies. Catalytic performance of the electrocatalysts for ECR and the products selectivity have been widely reported to be depended on the nanoparticle size effects (Birhanu et al., 2018; Xie et al., 2018; Nitopi et al., 2019). On the one hand, the decrease in nanoparticle size would increase the surface to bulk atom ratio and more surface defects are exposed for enhanced ECR activity (Stephens et al., 2012; Nitopi et al., 2019). On the other side, the active sites of NPs play different roles in determining the product distribution. The edge sites favor the formation of CO, while the corner sites promote HER (Birhanu et al., 2018). Smaller particle size indicates a lower coordination degree of the surface atoms. Hence, more low-coordinated surface sites are available for enhanced activities of the catalysts with smaller average particle size (Chen et al., 2013; Chen et al., 2017). For Cu-based catalysts, NPs with smaller nanoparticle sizes can afford low-coordinated active sites for facilitated production of CO and H_2, while the yield of C_{2+} products will be suppressed. In contrast, NPs with greater particle sizes will exhibit high selectivity toward the formation of CH_4 and other C_{2+} products (Reske et al., 2014; Nitopi et al., 2019). Therefore, the high FE_{CO} for the desired CuO-PVP catalyst should be associated with the enriched low-coordinated edge active sites due to its small particle size.

The particle size effect on the catalytic activity and products selectivity of nanostructured catalysts for electrochemical CO_2 reduction has been well understood. On the one hand, a tiny change in particle size will result in remarkable changes in the electronic structure of the catalysts, i.e., the shift of d-band, due to the strains induced on the surface atoms. This will in turn influence the catalytic activity (Hammer et al., 1996; Li et al., 2013c; Nitopi et al., 2019). On the other hand, the atom coordination density would be affected by the catalyst size. The decrease in particle size will result in the increase in the surface to bulk atom ratio, and the surface curvature increases, and the average coordination of the surface atoms will be lowered (Nitopi et al., 2019; Ni et al., 2021). In other words, the decreased particle size will induce the higher occurrence of undercoordinated sites, which will further influence the binding strength of the intermediate (Gao et al., 2019). Reske et al. reported that the products selectivity of Cu NPs in electrochemical CO_2 reduction depended heavily on their average particle size. As the average particle size of Cu NPs decreased from 15 to 2 nm, the population of low-coordinated surface sites (coordination number <8) increased (Reske et al., 2014). The enriched undercoordinated sites that showed strong chemical adsorption were beneficial for lowering the mobility of the *CO intermediate on the surface, and the transform of *CO to hydrocarbons was suppressed, and the selectivity towards CO and H_2 therefore had been boosted (Reske et al., 2014; Loiudice et al., 2016; Birdja et al., 2019). As the average particle size exceeded 25 nm, the formation of CO and H_2 was hindered and the production of hydrocarbons of CH_4 and C_2H_4 had been facilitated (Reske et al., 2014). Yin et al. prepared Cu_3N structure for selective electrochemical CO_2 reduction to ethylene. As the particle size of Cu_3N structure increased from 10 to 25 nm, CO_2RR selectivity to C_2H_4 increased from 34 to 57%, when the catalyst was tested at −1.6 V vs. RHE (Yin et al., 2019). Loiudice et al. synthesized Cu nanocrystals (NCs) of varied sizes (24 nm, 44 and 63 nm) for CO_2RR to C2 product, and the particle size effect on the CO_2 electroreduction activity and product selectivity was illustrated. The Cu NCs with an average particle size of 44 nm exhibited the highest C_2H_4 selectivity (41%) at −1.1 V vs. RHE. A further increase in particle size to 63 nm had resulted in the reduction in the ratio of edge sites to planar sites, and the C_2H_4 selectivity declined significantly to 25% (Loiudice et al., 2016). These indicate that the catalytic activity and products selectivity of copper-based catalysts depend on the undercoordinated sites due to the particle size effect. In previous work, we have prepared CuO catalysts with varied particle size by regulating the calcination temperature. Effect of calcination temperature on particle size, oxygen vacancy defects and electrochemical CO_2RR performance had been illustrated. Results indicated that a higher temperature would result in CuO catalyst with larger particle size and declined oxygen vacancy concentration. Particularly, as particle size of CuO catalyst increased, the selectivity towards CO and H_2 production slightly decreased, while the CO_2RR selectivity to methanol and ethanol increased. This had been associated with the particle size effect, since the increased particle size had caused the decrease in the density of the undercoordinated sites (Yao et al., 2021).

Oxygen-vacancy defects play important roles in promoting the adsorption and activation of CO_2 on metal oxide catalysts in ECR process. It is indicated that the concentration of oxygen vacancies in metal oxide catalysts will affect their electronic properties and electrochemical activities (Geng et al., 2018; Deng et al., 2020). Gao et al. reported that oxygen vacancies were the primary defect sites in cobalt oxide for ECR to formate (Gao et al., 2017). As proton transfer was the rate-limiting step, oxygen vacancies worked satisfactorily in lowering the rate-limiting activation barrier by stabilizing the formate anion radical intermediate. The OVs-rich and OVs-poor catalysts therefore exhibited distinct FEs of 87.6 and 67.3% for formate production under −0.23 V vs. RHE (Gao et al., 2017). Efforts therefore have been devoted to engineer the electronic properties for improved ECR performance by introducing more oxygen vacancies into the metal oxides catalysts (Geng et al., 2018). Geng et al. reported

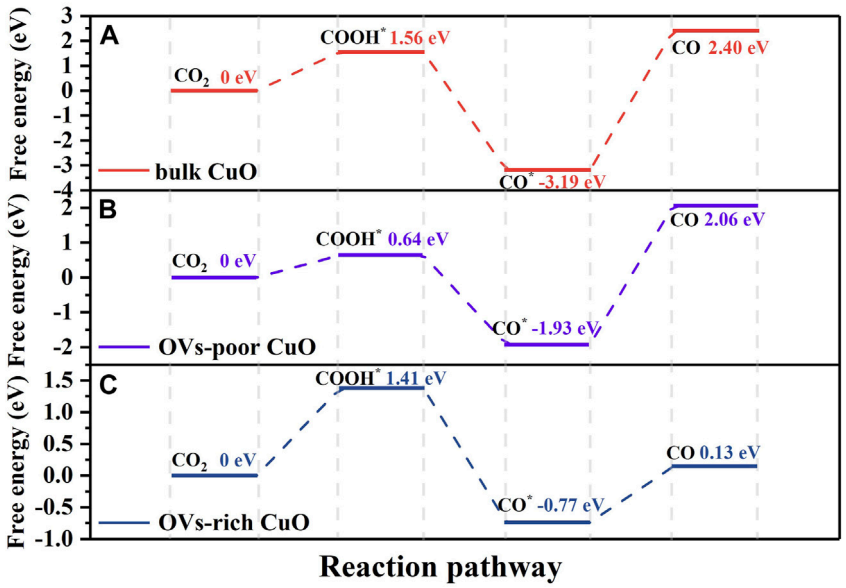

FIGURE 9 | Reaction free energy diagram toward various intermediates on the (111) facet of **(A)** bulk CuO, **(B)** OVs-poor CuO, and **(C)** OVs-rich CuO.

that the introduction of oxygen vacancies into ZnO nanosheets increased the charge density of ZnO to promote CO_2 activation, and this would improve their catalytic performance in ECR to CO. The OVs-rich ZnO catalyst exhibited high activity (j_{CO} = −16.1 mA/cm^2) and excellent selectivity (FE_{CO} = 83%) for ECR to CO production (Geng et al., 2018). Heat treatment, irradiation and doping modification could be efficient strategies for introducing oxygen vacancy defects into metal oxide catalysts of ZnO, $BiVO_4$ and MO_3 (Liu et al., 2016; Wang et al., 2017; Feng et al., 2020). It is widely acknowledged that the ECR to CO process over Cu-based catalysts involves several steps, and the first but the most important step is the adsorption and activation of CO_2 on the desired facets to form the key intermediate of COOH*. However, CO_2 adsorption and activation and the stabilization of the key intermediate have been reported depending on OVs concentrations (Gu et al., 2019; Karapinar et al., 2021). Herein, we report that the different templates employed in hydrothermal synthesis will affect the oxygen vacancies in the CuO nanostructures. Therefore, the relatively higher CO_2RR activity and CO selectivity of CuO-PVP and CuO-SDS should be associated with their relatively higher OVs concentration. Besides, the better performance in CO_2RR to CO should also be associated with their small particle size, considering the enriched undercoordinated sites for promoted CO production.

To elucidate the promoting role of oxygen vacancy defects in ECR, we have done DFT calculations to provide a theoretical insight into the pathways of CO_2RR on the (111) facets of bulk CuO, OVs-poor CuO and OVs-rich CuO catalysts. It is widely recognized that the CO_2RR to CO involves three steps: CO_2 activation to form COOH*, surface reaction of COOH* to form CO* and the desorption of CO from catalyst surface (Li et al., 2013b; Huang et al., 2017; Zhu et al., 2018; Gao et al., 2020). **Figure 9** shows the free energy diagrams for CO_2RR to CO on CuO catalysts through the COOH* generating pathway. Top views of the optimized structures of the catalysts and the main adsorption configurations of COOH* and CO* on the (111) facets of bulk CuO, OVs-poor CuO and OVs-rich CuO are presented in **Supplementary Figures S7–9**. The Gibbs free energies for the formation of COOH* on OVs-poor CuO and OVs-rich CuO are lower than that on bulk CuO, which indicates that the presence of OVs in CuO nanostructures reduces the activation barrier of CO_2 to COOH*. The Gibbs free energies for CO_2 activation on OVs-poor CuO and OVs-rich CuO decreases by 0.92 and 0.15 eV, with respect to the bulk CuO catalyst. The presence of OVs also affect the CO desorption process. Although the Gibbs free energies are uphill for the desorption of CO, the free energy for CO desorption on the (111) facet has been reduced for CuO with OVs. This is especially true for the OVs-rich CuO catalyst, since its free energy has been significantly reduced to 0.13 eV, compared to that of 2.40 eV required for CO desorption from the (111) facet of bulk CuO. This indicates that the CO adsorption strength on CuO with OVs is weaker than on the surface of CuO without OVs. Thus, OVs play important roles in not only promoting CO_2 activation but also facilitating CO desorption from the surface of CuO catalyst. The promoting role of OVs in CO_2RR has also been highlighted in open documents. Geng et al. reported that the introduction of OVs into ZnO nanosheet had decreased the Gibbs free energy for CO_2 activation by 0.28 eV, and this resulted in fast kinetics for CO_2RR to CO (Geng et al., 2018). Devi et al. demonstrated that the increase in the concentration of OV defects in the $Cu_{17}In_3O_{15}$ composite had decreased its CO_2 activation barrier from 0.48 to 0.31 eV for CO production, and this corresponded to the high CO faradaic efficiency of 85% at −0.895 V vs. RHE (Devi et al., 2019). Overall, the relatively better performance of CuO-PVP and CuO-SDS with higher OVs

concentration for CO_2RR to CO should be associated with the dual functionality of OVs in promoting CO_2 activation and facilitating CO desorption.

CONCLUSION

Nanostructured CuO catalysts were prepared via the template-assisted hydrothermal synthesis method using different templates for electrochemical CO_2 reduction to CO. Template effects on the structure-property-activity relationships of the CuO nanostructures were investigated by combining the results of electrochemical measurement, characterizations and DFT calculations. The different structures of the templates employed in hydrothermal synthesis have endowed the as-prepared CuO nanostructures with varied particle sizes and oxygen vacancy concentrations. Amongst, CuO-PVP and CuO-SDS showed smaller particle sizes and higher oxygen vacancy concentrations. The desired CuO-PVP and CuO-SDS catalysts exhibited good electrochemical performance with high $j_{CO\text{-}ECSA}$ of 2.21 and 1.37 mA/cm^2 and great FE_{CO} of 48.2 and 50.5% under the given potential of −0.93 V vs. RHE. The good CO_2 reduction activity and CO selectivity were associated with the particle size effect and the promoting role of the oxygen vacancy. CuO catalysts with smaller particle sizes could provide more low-coordinated defect sites for facilitated CO_2 adsorption and activation. DFT calculation results confirmed that the enriched oxygen vacancies in CuO nanostructures possessed a double functionality, namely, to promote CO_2 adsorption and activation, and to facilitate CO desorption from the catalyst surface. These results will provide significant instructions for designing robust and efficient catalysts for electrochemical CO_2 reduction. More efforts will be devoted to engineering the oxygen vacancy of the desired CuO catalysts via plasma treatment or metal oxide doping for boosted electrochemical performance.

DATA AVAILABILITY STATEMENT

The raw data supporting the conclusion of this article will be made available by the authors, without undue reservation.

AUTHOR CONTRIBUTIONS

XY: Conceptualization, Methodology, Investigation, Data curation, Writing—original draft; YJ: Visualization, Data curation, Formal analysis; XC: Investigation, Data curation, Formal analysis; BG: Investigation, Data curation, Formal analysis; SM: Conceptualization, Methodology, Investigation; YG: Conceptualization, Conceptualization, Funding acquisition, Writing—review and editing, Supervision; CZ: Conceptualization, Methodology, Investigation, Data curation.

FUNDING

The authors appreciate the National Natural Science Foundation of China (51806108), and the Natural Science Foundation of Jiangsu Province (BK20200731) for financial support.

SUPPLEMENTARY MATERIAL

The Supplementary Material for this article can be found online at: https://www.frontiersin.org/articles/10.3389/fenrg.2022.964011/full#supplementary-material

REFERENCES

Abdi, F. F., and van de Krol, R. (2012). Nature and Light Dependence of Bulk Recombination in Co-pi-catalyzed $BiVO_4$ Photoanodes. *J. Phys. Chem. C* 116, 9398–9404. doi:10.1021/jp3007552

Al-Hashem, M., Akbar, S., and Morris, P. (2019). Role of Oxygen Vacancies in Nanostructured Metal-Oxide Gas Sensors: A Review. *Sensors Actuators B Chem.* 301, 126845. doi:10.1016/j.snb.2019.126845

Birdja, Y. Y., Pérez-Gallent, E., Figueiredo, M. C., Göttle, A. J., Calle-Vallejo, F., and Koper, M. T. M. (2019). Advances and Challenges in Understanding the Electrocatalytic Conversion of Carbon Dioxide to Fuels. *Nat. Energy* 4, 732–745. doi:10.1038/s41560-019-0450-y

Birhanu, M. K., Tsai, M.-C., Kahsay, A. W., Chen, C.-T., Zeleke, T. S., Ibrahim, K. B., et al. (2018). Copper and Copper-Based Bimetallic Catalysts for Carbon Dioxide Electroreduction. *Adv. Mat. Interfaces* 5, 1800919. doi:10.1002/admi.201800919

Chaibundit, C., Ricardo, N. M. P. S., Costa, F. d. M. L. L., Yeates, S. G., and Booth, C. (2007). Micellization and Gelation of Mixed Copolymers P123 and F127 in Aqueous Solution. *Langmuir* 23, 9229–9236. doi:10.1021/la701157j

Chen, K., Deng, J., Zhao, J., Liu, X., Imhanria, S., and Wang, W. (2021). Electrocatalytic Production of Tunable Syngas from CO_2 via a Metal-free Porous Nitrogen-Doped Carbon. *Ind. Eng. Chem. Res.* 60, 7739–7745. doi:10.1021/acs.iecr.1c00779

Chen, K., Zhang, X., Williams, T., Bourgeois, L., and MacFarlane, D. R. (2017). Electrochemical Reduction of CO_2 on Core-Shell Cu/Au Nanostructure Arrays for Syngas Production. *Electrochimica Acta* 239, 84–89. doi:10.1016/j.electacta.2017.04.019

Dai, C., Qiu, Y., He, Y., Zhang, Q., Liu, R., Du, J., et al. (2019). Controlled Synthesis of a Bi_2O_3-CuO Catalyst for Selective Electrochemical Reduction of CO_2 to Formate. *New J. Chem.* 43, 3493–3499. doi:10.1039/c8nj05205k

Deng, Z., Ji, J., Xing, M., and Zhang, J. (2020). The Role of Oxygen Defects in Metal Oxides for CO_2 Reduction. *Nanoscale Adv.* 2, 4986. doi:10.1039/D0NA00535E

Devi, P., Malik, K., Arora, E., Bhattacharya, S., Kalendra, V., Lakshmi, K. V., et al. (2019). Selective Electrochemical Reduction of CO_2 to CO on CuO/In_2O_3 Nanocomposites: Role of Oxygen Vacancies. *Catal. Sci. Technol.* 9, 5339–5349. doi:10.1039/c9cy01396b

Dongare, S., Singh, N., and Bhunia, H. (2020). Nitrogen-doped Graphene Supported Copper Nanoparticles for Electrochemical Reduction of CO_2. *J. CO2 Util.* 44, 101382. doi:10.1016/j.jcou.2020.101382

Dutta, A., Rahaman, M., Luedi, N. C., Mohos, M., and Broekmann, P. (2016). Morphology Matters: Tuning the Product Distribution of CO_2 Electroreduction on Oxide-Derived Cu Foam Catalysts. *ACS Catal.* 6, 3804–3814. doi:10.1021/acscatal.6b00770

Dutta, A., Rahaman, M., Mohos, M., Zanetti, A., and Broekmann, P. (2017). Electrochemical CO_2 Conversion Using Skeleton (Sponge) Type of Cu Catalysts. *ACS Catal.* 7, 5431–5437. doi:10.1021/acscatal.7b01548

Feng, S., Wang, T., Liu, B., Hu, C., Li, L., Zhao, Z. J., et al. (2020). Enriched Surface Oxygen Vacancies of Photoanodes by Photoetching with Enhanced Charge Separation. *Angew. Chem. Int. Ed.* 59, 2044–2048. doi:10.1002/anie.201913295

Gao, D., Arán-Ais, R. M., Jeon, H. S., and Roldan Cuenya, B. (2019). Rational Catalyst and Electrolyte Design for CO_2 Electroreduction towards Multicarbon Products. *Nat. Catal.* 2, 198–210. doi:10.1038/s41929-019-0235-5

Gao, S., Sun, Z., Liu, W., Jiao, X., Zu, X., Hu, Q., et al. (2017). Atomic Layer Confined Vacancies for Atomic-Level Insights into Carbon Dioxide Electroreduction. *Nat. Commun.* 8, 1–9. doi:10.1038/ncomms14503

Gao, Y., Wu, Q., Liang, X., Wang, Z., Zheng, Z., Wang, P., et al. (2020). Cu_2O Nanoparticles with Both {100} and {111} Facets for Enhancing the Selectivity and Activity of CO_2 Electroreduction to Ethylene. *Adv. Sci.* 7, 1902820. doi:10.1002/advs.201902820

Gattrell, M., Gupta, N., and Co, A. (2007). Electrochemical Reduction of CO_2 to Hydrocarbons to Store Renewable Electrical Energy and Upgrade Biogas. *Energy Convers. Manag.* 48, 1255–1265. doi:10.1016/j.enconman.2006.09.019

Geng, Z., Kong, X., Chen, W., Su, H., Liu, Y., Cai, F., et al. (2018). Oxygen Vacancies in ZnO Nanosheets Enhance CO_2 Electrochemical Reduction to CO. *Angew. Chem.* 130, 6162–6167. doi:10.1002/ange.201711255

Gu, Z., Shen, H., Shang, L., Lv, X., Qian, L., and Zheng, G. (2018). Nanostructured Copper-Based Electrocatalysts for CO_2 Reduction. *Small Methods* 2, 1800121. doi:10.1002/smtd.201800121

Gu, Z., Yang, N., Han, P., Kuang, M., Mei, B., Jiang, Z., et al. (2019). Oxygen Vacancy Tuning toward Efficient Electrocatalytic CO_2 Reduction to C_2H_4. *Small Methods* 3, 1800449.

Guo, Y., Tan, C., Sun, J., Li, W., Zhang, J., and Zhao, C. (2020). Porous Activated Carbons Derived from Waste Sugarcane Bagasse for CO_2 Adsorption. *Chem. Eng. J.* 381, 122736. doi:10.1016/j.cej.2019.122736

Guo, Y., Tan, C., Wang, P., Sun, J., Li, W., Zhao, C., et al. (2020). Structure-performance Relationships of Magnesium-Based CO_2 Adsorbents Prepared with Different Methods. *Chem. Eng. J.* 379, 122277. doi:10.1016/j.cej.2019.122277

Hammer, B., Morikawa, Y., and Nørskov, J. K. (1996). CO Chemisorption at Metal Surfaces and Overlayers. *Phys. Rev. Lett.* 76, 2141–2144. doi:10.1103/physrevlett.76.2141

Han, H., Jin, S., Park, S., Kim, Y., Jang, D., Seo, M. H., et al. (2021). Plasma-induced Oxygen Vacancies in Amorphous MnOx Boost Catalytic Performance for Electrochemical CO_2 Reduction. *Nano Energy* 79, 105492. doi:10.1016/j.nanoen.2020.105492

Han, N., Wang, Y., Ma, L., Wen, J., Li, J., Zheng, H., et al. (2017). Supported Cobalt Polyphthalocyanine for High-Performance Electrocatalytic CO_2 Reduction. *Chem* 3, 652–664. doi:10.1016/j.chempr.2017.08.002

He, Q., Lee, J. H., Liu, D., Liu, Y., Lin, Z., Xie, Z., et al. (2020). Accelerating CO_2 Electroreduction to CO over Pd Single-Atom Catalyst. *Adv. Funct. Mat.* 30, 2000407. doi:10.1002/adfm.202000407

Hori, Y., Murata, A., and Takahashi, R. (1989). Formation of Hydrocarbons in the Electrochemical Reduction of Carbon Dioxide at a Copper Electrode in Aqueous Solution. *J. Chem. Soc. Faraday Trans. 1* 85, 2309–2326. doi:10.1039/f19898502309

Hori, Y., Takahashi, I., Koga, O., and Hoshi, N. (2003). Electrochemical Reduction of Carbon Dioxide at Various Series of Copper Single Crystal Electrodes. *J. Mol. Catal. A Chem.* 199, 39–47. doi:10.1016/s1381-1169(03)00016-5

Huang, P., Ci, S., Wang, G., Jia, J., Xu, J., and Wen, Z. (2017). High-activity Cu Nanowires Electrocatalysts for CO_2 Reduction. *J. CO2 Util.* 20, 27–33. doi:10.1016/j.jcou.2017.05.002

Iyengar, P., Huang, J., De Gregorio, G. L., Gadiyar, C., and Buonsanti, R. (2019). Size Dependent Selectivity of Cu Nano-Octahedra Catalysts for the Electrochemical Reduction of CO_2 to CH_4. *Chem. Commun.* 55, 8796–8799. doi:10.1039/c9cc02522g

Jhong, H. R. M., Ma, S., and Kenis, P. J. (2013). Electrochemical Conversion of CO_2 to Useful Chemicals: Current Status, Remaining Challenges, and Future Opportunities. *Curr. Opin. Chem. Eng.* 2, 191–199. doi:10.1016/j.coche.2013.03.005

Jiang, F., Wang, S., Liu, B., Liu, J., Wang, L., Xiao, Y., et al. (2020). Insights into the Influence of CeO_2 Crystal Facet on CO_2 Hydrogenation to Methanol over Pd/CeO_2 Catalysts. *ACS Catal.* 10, 11493–11509. doi:10.1021/acscatal.0c03324

Jiang, Y., Choi, C., Hong, S., Chu, S., Wu, T.-S., Soo, Y.-L., et al. (2021). Enhanced Electrochemical CO_2 Reduction to Ethylene over CuO by Synergistically Tuning Oxygen Vacancies and Metal Doping. *Cell Rep. Phys. Sci.* 2, 100356. doi:10.1016/j.xcrp.2021.100356

Karapinar, D., Creissen, C. E., Rivera de la Cruz, J. G., Schreiber, M. W., and Fontecave, M. (2021). Electrochemical CO_2 Reduction to Ethanol with Copper-Based Catalysts. *ACS Energy Lett.* 6, 694–706. doi:10.1021/acsenergylett.0c02610

Koczkur, K. M., Mourdikoudis, S., Polavarapu, L., and Skrabalak, S. E. (2015). Polyvinylpyrrolidone (PVP) in Nanoparticle Synthesis. *Dalton Trans.* 44, 17883–17905. doi:10.1039/c5dt02964c

Kou, W., Zhang, Y., Dong, J., Mu, C., and Xu, L. (2020). Nickel-Nitrogen-Doped Three-Dimensional Ordered Macro-/Mesoporous Carbon as an Efficient Electrocatalyst for CO_2 Reduction to CO. *ACS Appl. Energy Mat.* 3, 1875–1882. doi:10.1021/acsaem.9b02324

Kuhl, K. P., Cave, E. R., Abram, D. N., and Jaramillo, T. F. (2012). New Insights into the Electrochemical Reduction of Carbon Dioxide on Metallic Copper Surfaces. *Energy Environ. Sci.* 5, 7050–7059. doi:10.1039/c2ee21234j

Kuo, C.-H., Chiang, T.-F., Chen, L.-J., and Huang, M. H. (2004). Synthesis of Highly Faceted Pentagonal- and Hexagonal-Shaped Gold Nanoparticles with Controlled Sizes by Sodium Dodecyl Sulfate. *Langmuir* 20, 7820–7824. doi:10.1021/la049172q

Larrazábal, G. n. O., Martín, A. J., and Pérez-Ramírez, J. (2017). Building Blocks for High Performance in Electrocatalytic CO_2 Reduction: Materials, Optimization Strategies, and Device Engineering. *J. Phys. Chem. Lett.* 8, 3933–3944. doi:10.1021/acs.jpclett.7b01380

Li, C. W., and Kanan, M. W. (2012). CO_2 Reduction at Low Overpotential on Cu Electrodes Resulting from the Reduction of Thick Cu_2O Films. *J. Am. Chem. Soc.* 134, 7231–7234. doi:10.1021/ja3010978

Li, J., Li, Y., Lee, T.-C., and Huang, Q. (2013). Structure and Physical Properties of Zein/Pluronic F127 Composite Films. *J. Agric. Food Chem.* 61, 1309–1318. doi:10.1021/jf3043055

Li, L., Cheah, Y., Ko, Y., Teh, P., Wee, G., Wong, C., et al. (2013). The Facile Synthesis of Hierarchical Porous Flower-like $NiCo_2O_4$ with Superior Lithium Storage Properties†. *J. Mater. Chem. A* 1, 10935–10941. doi:10.1039/c3ta11549f

Li, L., Larsen, A. H., Romero, N. A., Morozov, V. A., Glinsvad, C., Abild-Pedersen, F., et al. (2013). Investigation of Catalytic Finite-Size-Effects of Platinum Metal Clusters. *J. Phys. Chem. Lett.* 4, 222–226. doi:10.1021/jz3018286

Liu, B., Yao, X., Zhang, Z., Li, C., Zhang, J., Wang, P., et al. (2021). Synthesis of Cu_2O Nanostructures with Tunable Crystal Facets for Electrochemical CO_2 Reduction to Alcohols. *ACS Appl. Mat. Interfaces* 13, 39165–39177. doi:10.1021/acsami.1c03850

Chen, X., Liu, K., Li, Y., and Lv, M. (2013). Synthesis and Electrochemical Performance of Ball-in-Ball Structure LiFePO4/C. *Battery* 43, 136–138. (in Chinese)

Liu, K., Zhang, W., Lei, F., Liang, L., Gu, B., Sun, Y., et al. (2016). Nitrogen-doping Induced Oxygen Divacancies in Freestanding Molybdenum Trioxide Single-Layers Boosting Electrocatalytic Hydrogen Evolution. *Nano Energy* 30, 810–817. doi:10.1016/j.nanoen.2016.09.015

Liu, S.-Q., Wu, S.-W., Gao, M.-R., Li, M.-S., Fu, X.-Z., and Luo, J.-L. (2019). Hollow Porous Ag Spherical Catalysts for Highly Efficient and Selective Electrocatalytic Reduction of CO_2 to CO. *ACS Sustain. Chem. Eng.* 7, 14443–14450. doi:10.1021/acssuschemeng.9b01635

Loiudice, A., Lobaccaro, P., Kamali, E. A., Thao, T., Huang, B. H., Ager, J. W., et al. (2016). Tailoring Copper Nanocrystals towards C_2 Products in Electrochemical CO_2 Reduction. *Angew. Chem. Int. Ed.* 55, 5789–5792. doi:10.1002/anie.201601582

Lu, W., Zhang, Y., Zhang, J., and Xu, P. (2020). Reduction of Gas CO_2 to CO with High Selectivity by Ag Nanocube-Based Membrane Cathodes in a Photoelectrochemical System. *Ind. Eng. Chem. Res.* 59, 5536–5545. doi:10.1021/acs.iecr.9b06052

Ma, M., Djanashvili, K., and Smith, W. A. (2015). Selective Electrochemical Reduction of CO_2 to CO on CuO-Derived Cu Nanowires. *Phys. Chem. Chem. Phys.* 17, 20861–20867. doi:10.1039/c5cp03559g

Mac Dowell, N., Fennell, P. S., Shah, N., and Maitland, G. C. (2017). The Role of CO_2 Capture and Utilization in Mitigating Climate Change. *Nat. Clim. Change* 7, 243–249. doi:10.1038/nclimate3231

Ni, Z., Liang, H., Yi, Z., Guo, R., Liu, C., Liu, Y., et al. (2021). Research Progress of Electrochemical CO_2 Reduction for Copper-Based Catalysts to Multicarbon Products. *Coord. Chem. Rev.* 441, 213983. doi:10.1016/j.ccr.2021.213983

Nitopi, S., Bertheussen, E., Scott, S. B., Liu, X., Engstfeld, A. K., Horch, S., et al. (2019). Progress and Perspectives of Electrochemical CO_2 Reduction on Copper in Aqueous Electrolyte. *Chem. Rev.* 119, 7610–7672. doi:10.1021/acs.chemrev.8b00705

Peng, X., Karakalos, S. G., and Mustain, W. E. (2018). Preferentially Oriented Ag Nanocrystals with Extremely High Activity and Faradaic Efficiency for CO_2 Electrochemical Reduction to CO. *ACS Appl. Mat. Interfaces* 10, 1734–1742. doi:10.1021/acsami.7b16164

Polak, D., Sułkowska, J., and Szwast, M. (2021). The Influence of Surfactant Pluronic P123 Addition on the Mixed Matrix Membrane PEBAX 2533 - ZIF-8 Separation Properties. *Desalination Water Treat.* 214, 64–73. doi:10.5004/dwt.2021.26647

Reske, R., Mistry, H., Behafarid, F., Roldan Cuenya, B., and Strasser, P. (2014). Particle Size Effects in the Catalytic Electroreduction of CO_2 on Cu Nanoparticles. *J. Am. Chem. Soc.* 136, 6978–6986. doi:10.1021/ja500328k

Shu, D., Cheng, H., Lv, C., Asi, M. A., Long, L., He, C., et al. (2014). Soft-template Synthesis of Vanadium Oxynitride-Carbon Nanomaterials for Supercapacitors. *Int. J. Hydrogen Energy* 39, 16139–16150. doi:10.1016/j.ijhydene.2014.05.119

Sing, K. S. W. (1985). Reporting Physisorption Data for Gas/solid Systems with Special Reference to the Determination of Surface Area and Porosity (Recommendations 1984). *Pure Appl. Chem.* 57, 603–619. doi:10.1351/pac198557040603

Stephens, I. E. L., Bondarenko, A. S., Grønbjerg, U., Rossmeisl, J., and Chorkendorff, I. (2012). Understanding the Electrocatalysis of Oxygen Reduction on Platinum and its Alloys. *Energy Environ. Sci.* 5, 6744–6762. doi:10.1039/c2ee03590a

Sun, Z., Ma, T., Tao, H., Fan, Q., and Han, B. (2017). Fundamentals and Challenges of Electrochemical CO_2 Reduction Using Two-Dimensional Materials. *Chem* 3, 560–587. doi:10.1016/j.chempr.2017.09.009

Tan, D., Zhang, J., Yao, L., Tan, X., Cheng, X., Wan, Q., et al. (2020). Multi-shelled CuO Microboxes for Carbon Dioxide Reduction to Ethylene. *Nano Res.* 13, 768–774. doi:10.1007/s12274-020-2692-1

Tang, W., Peterson, A. A., Varela, A. S., Jovanov, Z. P., Bech, L., Durand, W. J., et al. (2012). The Importance of Surface Morphology in Controlling the Selectivity of Polycrystalline Copper for CO_2 Electroreduction. *Phys. Chem. Chem. Phys.* 14, 76–81. doi:10.1039/c1cp22700a

Wang, R., Jiang, R., Dong, C., Tong, T., Li, Z., Liu, H., et al. (2021). Engineering a Cu/ZnOx Interface for High Methane Selectivity in CO_2 Electrochemical Reduction. *Ind. Eng. Chem. Res.* 60, 273–280. doi:10.1021/acs.iecr.0c04718

Wang, W., Lu, R., Xiao, X., Gong, S., Sam, D. K., Liu, B., et al. (2021). CuAg Nanoparticle/carbon Aerogel for Electrochemical CO_2 Reduction. *New J. Chem.* 45, 18290–18295. doi:10.1039/d1nj03540a

Wang, Y., Niu, C., Zhu, Y., He, D., and Huang, W. (2020). Potassium-Ion Batteries: Key to Future Large-Scale Energy Storage? *ACS Appl. Energy Mat.* 3, 9478–9492.

Wang, Y., Wang, B., Xu, Y., Fang, M., Wu, Z., Zhu, W., et al. (2017). Hydrothermal Oxidation Synthesis of Rod-like ZnO and the Influence of Oxygen Vacancy on Photocatalysis. *J. Chin. Chem. Soc.* 64, 188–194. doi:10.1002/jccs.201600787

Woyessa, G. W., dela Cruz, J.-a. B., Rameez, M., and Hung, C.-H. (2021). Nanocomposite Catalyst of Graphitic Carbon Nitride and Cu/Fe Mixed Metal Oxide for Electrochemical CO_2 Reduction to CO. *Appl. Catal. B Environ.* 291, 120052. doi:10.1016/j.apcatb.2021.120052

Xiao, X., Xu, Y., Lv, X., Xie, J., Liu, J., and Yu, C. (2019). Electrochemical CO_2 Reduction on Copper Nanoparticles-Dispersed Carbon Aerogels. *J. Colloid Interface Sci.* 545, 1–7. doi:10.1016/j.jcis.2019.03.005

Xie, H., Wang, T., Liang, J., Li, Q., and Sun, S. (2018). Cu-based Nanocatalysts for Electrochemical Reduction of CO_2. *Nano Today* 21, 41–54. doi:10.1016/j.nantod.2018.05.001

Xu, B., Chen, D., Venkateshkumar, M., Xiao, Y., Yue, Y., Xing, Y., et al. (2019). Modeling a Pumped Storage Hydropower Integrated to a Hybrid Power System with Solar-Wind Power and its Stability Analysis. *Appl. Energy* 248, 446–462. doi:10.1016/j.apenergy.2019.04.125

Yang, D.-R., Liu, L., Zhang, Q., Shi, Y., Zhou, Y., Liu, C., et al. (2020). Importance of Au Nanostructures in CO_2 Electrochemical Reduction Reaction. *Sci. Bull.* 65, 796–802. doi:10.1016/j.scib.2020.01.015

Yang, Y., Ajmal, S., Zheng, X., and Zhang, L. (2018). Efficient Nanomaterials for Harvesting Clean Fuels from Electrochemical and Photoelectrochemical CO_2reduction. *Sustain. Energy Fuels* 2, 510–537. doi:10.1039/c7se00371d

Yao, X., Guo, Y., Liu, B., Wang, P., Sun, J., Li, W., et al. (2021). Syngas Production from Electrochemical CO_2 Reduction on Copper Oxide Electrodes in Aqueous Solution. *Chemelectrochem* 8, 592–602. doi:10.1002/celc.202001504

Yin, Z., Yu, C., Zhao, Z., Guo, X., Shen, M., Li, N., et al. (2019). Cu_3N Nanocubes for Selective Electrochemical Reduction of CO_2 to Ethylene. *Nano Lett.* 19, 8658–8663. doi:10.1021/acs.nanolett.9b03324

Zhang, F., Jin, Z., Chen, C., Tang, Y., Mahyoub, S. A., Yan, S., et al. (2020). Electrochemical Conversion of CO_2 to CO into a Microchannel Reactor System in the Case of Aqueous Electrolyte. *Ind. Eng. Chem. Res.* 59, 5664–5674. doi:10.1021/acs.iecr.9b07014

Zhang, M., Hu, Z., Gu, L., Zhang, Q., Zhang, L., Song, Q., et al. (2020). Electrochemical Conversion of CO_2 to Syngas with a Wide Range of CO/H_2 Ratio over Ni/Fe Binary Single-Atom Catalysts. *Nano Res.* 13, 3206–3211. doi:10.1007/s12274-020-2988-1

Zhao, M., Li, W., Li, J., Hu, W., and Li, C. M. (2020). Strong Electronic Interaction Enhanced Electrocatalysis of Metal Sulfide Clusters Embedded Metal-Organic Framework Ultrathin Nanosheets toward Highly Efficient Overall Water Splitting. *Adv. Sci.* 7, 2001965. doi:10.1002/advs.202001965

Zhu, W., Zhang, L., Yang, P., Chang, X., Dong, H., Li, A., et al. (2018). Morphological and Compositional Design of Pd-Cu Bimetallic Nanocatalysts with Controllable Product Selectivity toward CO_2 Electroreduction. *Small* 14, 1703314. doi:10.1002/smll.201703314

Zhuang, G., Chen, Y., Zhuang, Z., Yu, Y., and Yu, J. (2020). Oxygen. Vacancies in Metal Oxides: Recent Progress towards Advanced Catalyst Design. *Sci. China Mat.* 63, 2089–2118. doi:10.1007/s40843-40020-41305-40846

Conflict of Interest: XY, YJ, XC, BG, and SM were employed by the Sinopec Nanjing Chemical Industries Co., Ltd. XC, BG, and SM were employed by the Sinopec Nanjing Research Institute of Chemical Industry Co., Ltd.

The remaining authors declare that the research was conducted in the absence of any commercial or financial relationships that could be construed as a potential conflict of interest.

Publisher's Note: All claims expressed in this article are solely those of the authors and do not necessarily represent those of their affiliated organizations, or those of the publisher, the editors and the reviewers. Any product that may be evaluated in this article, or claim that may be made by its manufacturer, is not guaranteed or endorsed by the publisher.